Metastable chloride solid electrolyte with high formability for re-chargeable all-solid-state lithium metal batteries

Naoto Tanibata*[1,2], Shuta Takimoto[1], Koki Nakano[1], Hayami Takeda[1,2], Masanobu Nakayama[1,2,3], Hirofumi Sumi[4]

[1] Department of Advanced Ceramics, Nagoya Institute of Technology, Gokiso, Showa, Nagoya, Aichi 466-8555, Japan

[2] Elements Strategy Initiative for Catalysts and Batteries (ESICB), Kyoto University, 1-30 Goryo-Ohara, Nishikyo, Kyoto 615-8245, Japan

[3] Frontier Research Institute for Materials Science (FRIMS), Nagoya Institute of Technology, Gokiso, Showa, Nagoya, Aichi 466-8555, Japan

[4] Innovative Functional Materials Research Institute, National Institute of Advanced Industrial Science and Technology (AIST), 2266-98, Anagahora, Shimo-shidami, Moriyama-ku, Nagoya 463-8560, Japan

*Corresponding Author: tanibata.naoto@nitech.ac.jp

ABSTRACT: Dense solid electrolytes in all-solid-state Li batteries are expected to suppress Li dendrite phenomena that prevent the application of high-energy-density Li metal electrodes. However, voids and cracks in sintered electrolytes still permit short-circuiting due to Li dendrites. This study aimed to investigate solid electrolytes with high formability in which green compacts can prevent Li dendrites. Li^+ ion migration energies, bulk moduli, and energies above the hull were comprehensively investigated using first principles and classical force field calculations as the indicators for ionic conductivity, formability, and thermodynamic stability. The 231 compounds containing Li and Cl listed in the *Materials Project* database were studied due to their high polarizability and weak Coulombic interaction with Li^+ ions. Among them, monoclinic $LiAlCl_4$ (LAC, S.G.: $P12_{1/c}1$) was focused on, owing to its low values of all three indicators. A mechanochemical synthesis was attempted to prepare the metastable phase, where Li ions occupy the interstitial sites, not just the original sites, because the computation for the migration energy suggested conductive pathways between the original Li sites. XRD and ^{7}Li-MAS NMR measurements indicated that the mechanochemically synthesized LAC possessed a monoclinic host structure while 2.5% Li occupied interstitial tetrahedral sites. Impedance measurements showed that the LAC green compacts exhibited an ionic conductivity of 2.1×10^{-5} S cm^{-1}, 20 times higher than the conventional solid-state synthesized LAC at room temperature. The conductivity was more than one order of magnitude higher than that of garnet-type $Li_{6.6}La_3Zr_{1.6}Ta_{0.4}O_{12}$ (LLZT), which has been attractive for the application of the sintered body for Li metal electrodes. The SEM observations and distribution of relaxation times analysis indicated that dense LAC green compacts with large necking between the particles contributed minimal grain-boundary resistance (7.5%) to the total resistance, while the LLZT green compacts contributed almost completely (99%). Li metal symmetric cells using the LAC pellet showed good cycle performance without short-circuiting and an overvoltage increase for 70 cycles at a current density of 0.1 mA cm^{-2}, while short circuiting occurred at the 1st cycle in the LLZT cells.

Higher energy density and safety are required for Li ion batteries, especially those utilized for large-scale power sources such as in electric vehicles.[1] Li metal anodes are the most attractive choice for application in high-energy-density batteries owing to their low electronegativity and large theoretical capacity.[2,3] However, Li dendrite growth during the charging process has hindered their application, which causes short-circuiting and even leads to explosion of the cells in the worst-case scenario.[4,5] The application in large-scale power sources also introduces further risks accompanied with flammability and fluidity of the organic electrolyte solution in conventional Li ion batteries.[6] All-solid-state Li ion batteries, where non-flammable solid electrolytes are substituted for the electrolyte solutions, have become attractive owing to their reliability and the possibility of Li dendrite suppression.[7–9] Such batteries are called bulk-type all-solid-state batteries in contrast to the thin-film types with limited energy density. However, high resistances of the Li ion transfer in solid electrolytes and/or at insufficient contact between solid particles often deteriorate the battery's performance.[10–12] Good connection of solid-solid particles between solid electrolyte particles and/or between solid electrolyte/electrode particles in the batteries is generally formed by high-temperature sintering.[13,14] However, the process largely limits materials selection due to the element volatilization[15,16] and/or undesired side reaction at the solid electrolyte/electrode interface[17,18]. Moreover, curves and cracks of the multilayer batteries are produced due to the different thermal expansion coefficient of each material.[19,20] The cracks, in addition to small pores and weak grain boundaries in the solid electrolyte layer, contribute to short-circuit phenomena.[21–23] Therefore, non-sintered bulk-type all-solid-state batteries are desired, especially for the application of Li metal anodes.

In this study, chloride materials, rather than conventional oxide materials, are focused on to reveal a material with high formability, where only cold pressing forms a dense pellet inhibiting

Li dendrites by strong particle connections with fast ionic transfer. The host structure of the chloride ion with a larger ionic radius and more electrons than the oxide ion generally contribute to higher polarizability and formability of the powder.[24] Moreover, the lower electronegative charge density of the chloride ion, rather than the oxide ion, is expected to lead to high Li conductivity due to the weak Coulombic interaction of Li^+ ions with the host structure.[25] However, not all compounds containing Li and Cl elements can be thermodynamically stable and show high Li^+ ionic conductivity and formability. Hence, indicators of these properties were calculated comprehensively for the Li-Cl compounds listed in the *Materials Project* database[26]. Migration energy[27–29], bulk modulus[30], and energy above the convex hull[31] were assessed for ionic conductivity, formability, and thermodynamic stability, respectively. The details of the calculation method are explained in the Computational Methods section. **Figure 1(a)** shows these calculated indicators for the 231 Li-Cl compounds. Monoclinic $LiAlCl_4$ (LAC, mp-22983) was focused on due to its low value of all three indicators among the 231 compounds.

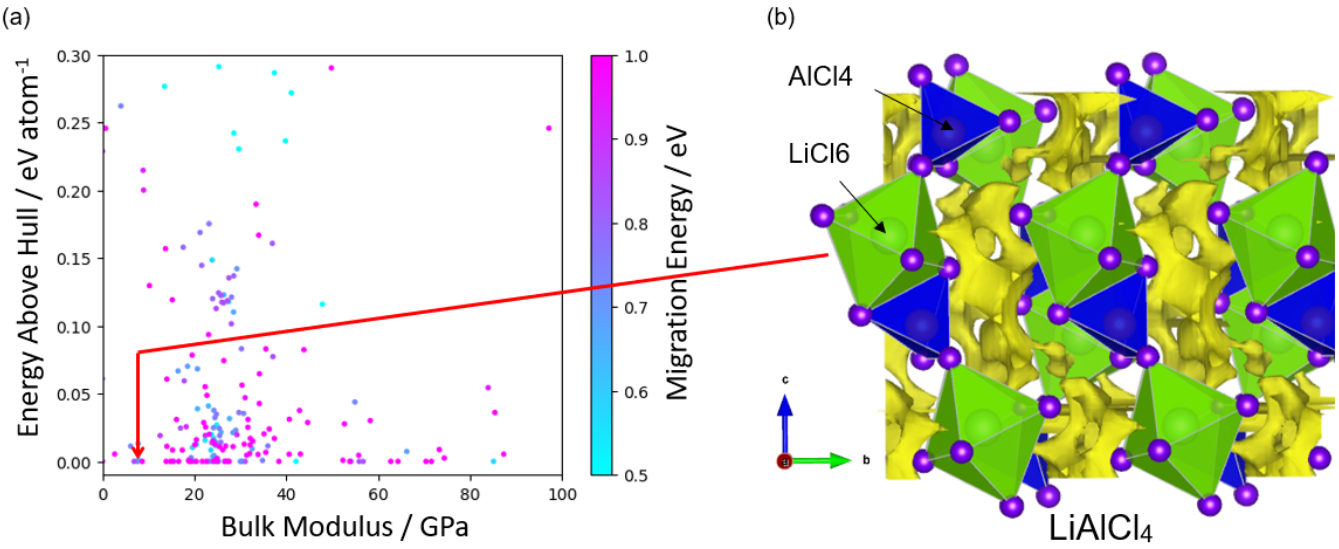

Figure 1. Results of computations to reveal battery materials suitable for non-sintered all-solid-state Li metal batteries. (a) Relationship among bulk modulus, energy above hull, and migration energy for 231 Li-Cl containing materials listed in the *Materials Project* database[26]. The crystal structures and energies above the hull were referred from the database. The bulk moduli were calculated by first-principles density functional theory (DFT) calculations. The migration energies were calculated based on bond valence force field[32] and automated pathway analyses based on percolation theory[27]. (b) Crystal structure of the monoclinic $LiAlCl_4$ (LAC) with low values of all three indicators among the 231 compounds. The yellow-colored iso-surfaces correspond to Li^+ ion chemical potential calculated by a force-field calculation.

Ionic conductivity of the monoclinic LAC synthesized by the solid-state reaction has been reported only by Weppner *et al.*.[33] The material is a thermodynamically stable compound up to the melting point of 146 °C.[34] Considering that the conductivity at room temperature is relatively low at 1×10^{-6} S cm^{-1}, the activation energy for ionic conductivity is not very high, at just 0.47 eV. For example, garnet-type $Li_7La_3Zr_2O_{12}$ (LLZO), which is a promising material due to its high Li^+ ion conductivity and compatibility with Li metal,[15,35] shows a conductivity one order of magnitude higher even the comparable activation energy of 0.47 eV by substituting Bi for Zr.[36] The ionic conduction in the LAC is supposed to be limited by some parameters except for the migration energy. The crystal structure and calculated conductive pathway shown in **Figure 1(b)** indicate that the compound has large space in the Li^+ ion conductive pathway. Li^+ ion delocalization between the original site and sites in the space would increase the Li^+ ion conductivity. Therefore, synthesis of the metastable LAC was attempted by a mechanochemical method for improving the Li^+ ion conductivity. In this study, the conductivity, formability, and dendrite inhibition ability of the powder-compressed pellet (green compact) were investigated.

The XRD pattern of the mechanochemically synthesized LAC is shown in **Figure 2(a)**. The peak positions agree with those of the monoclinic LAC structure (S.G.: $P12_{1/c}1$) reported in the ICSD database[37]. The ^{7}Li-MAS NMR spectra of the mechanochemically synthesized LAC in **Figure 2(c)** show a peak with a chemical shift of approximately 0 ppm, which is herein assigned as signal 1. A weak peak of signal 2 is also observed at approximately 1.6 ppm, which disappears as a result of annealing at 80 °C. The change by annealing indicates the mechanochemically synthesized LAC has a metastable phase. Signal 1 is attributed to Li^+ ions at the octahedral site shown in **Figure 2(b)** according to the former NMR study on Li containing spinel chlorides[38]. Since peak of signal 1 is only observed for annealed LAC, all of the Li ions are positioned at octahedral sites as reported Rietveld analysis for LAC[37]. The peaks at a slightly lower magnetic field have also been attributed to the tetrahedral

site Li^+ ions. In addition, tetrahedral sites are suggested as second-stable sites simulated by a force-field calculation, as shown in **Figure 2(b)**. Signal 2 is therefore attributed to the Li^+ ions at the metastable tetrahedral site. The integrated intensity ratio of signal 2 to signal 1 is 2.5%, calculated by using the Voigt function, shown in **Figure 2(d)**. These results indicate that a few percentages of Li^+ ions in the mechanochemically synthesized LAC are delocalized in the host structure of the room-temperature phase.

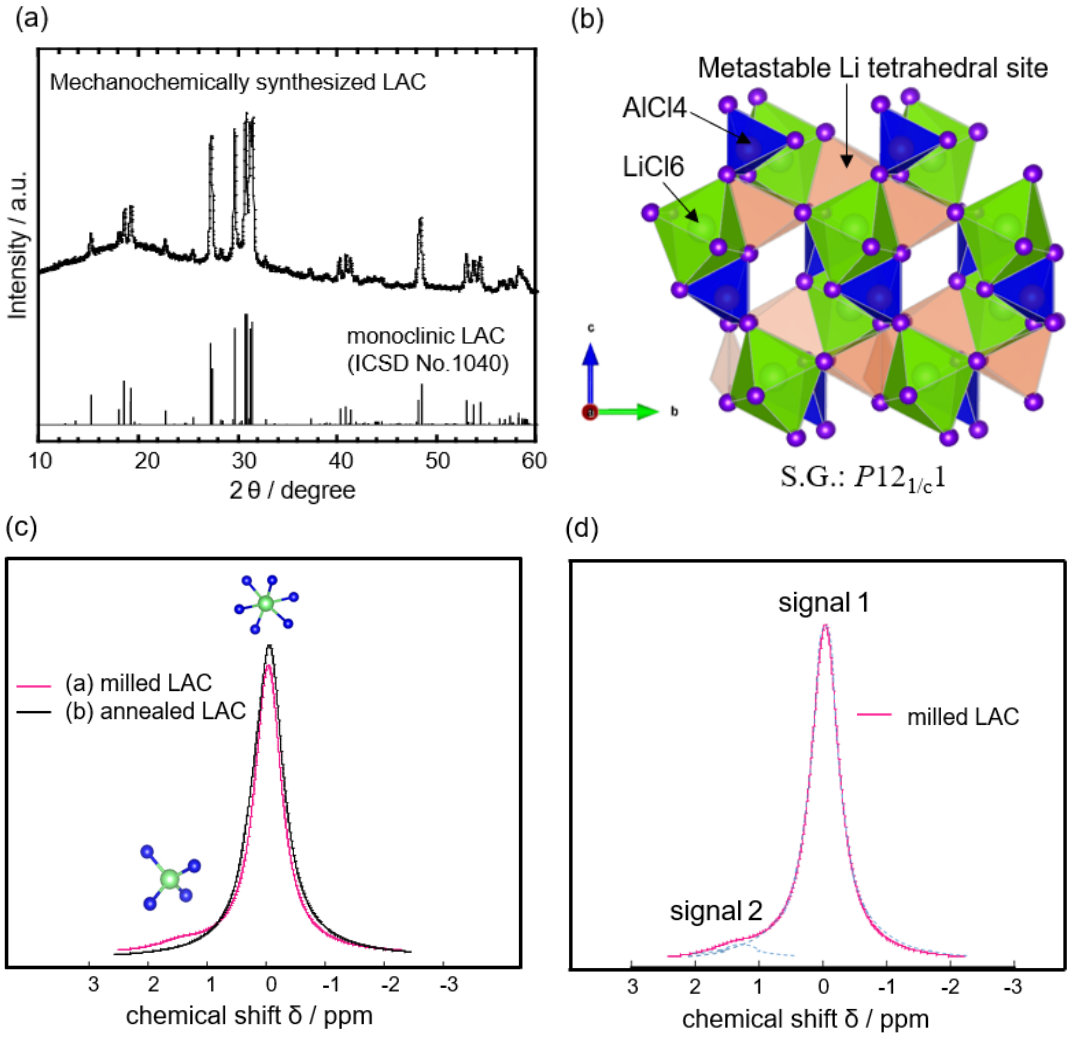

Figure 2. Characterization of $LiAlCl_4$ (LAC) powder. (a) XRD pattern of the mechanochemically synthesized LAC and simulated pattern of the monoclinic LAC reported in the ICSD database[37]. (b) Crystal structure of monoclinic LAC and second-stable Li site of tetrahedral site next to the octahedral site suggested by the bond valence force field (BVFF) approach[23]. (c) NMR spectra of the milled LAC and annealed LAC. (d) Peak fitting results for the spectrum of the milled LAC.

The cross-sectional SEM images and relative densities of the LAC and $Li_{6.6}La_3Zr_{1.6}Ta_{0.4}O_{12}$ (LLZT)[39] green compacts are shown in **Figure 3(a)** and **(b)**. The comparison LLZT is a representative oxide electrolyte for Li metal batteries, where the partial substitution of Ta for Zr has further improved the ionic conductivity of LLZO. The relative densities were calculated by using the apparent densities of the pellets, and crystal densities of monoclinic LAC and cubic LLZT. The LAC green compact shows a much higher relative density (94%) than the LLZT green compact (63%). Particles are connected by necking in the LAC green compact, although clear grain boundaries were observed in the LLZT green compact as expected for conventional oxides.

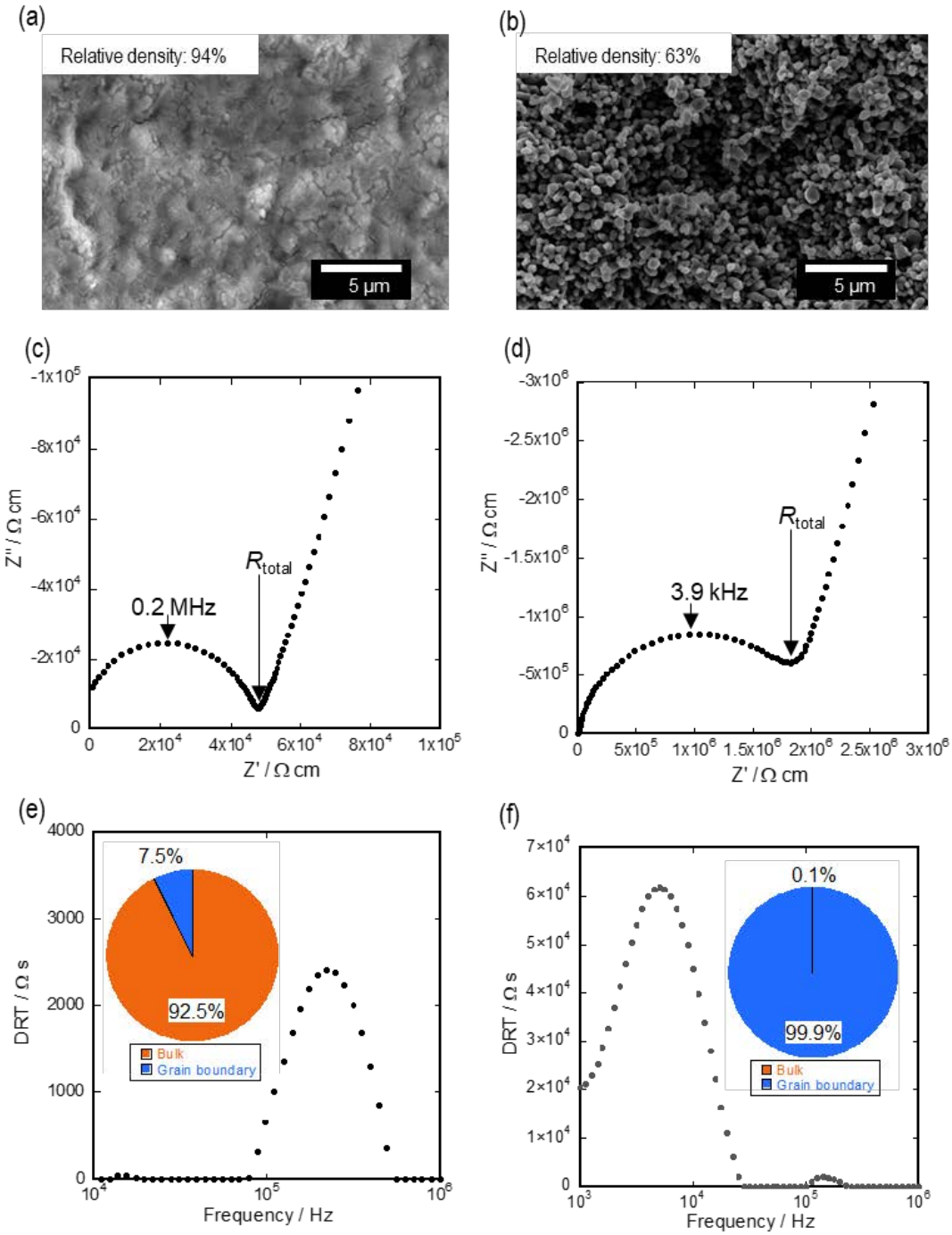

Figure 3. Characterization of the green compacts of $LiAlCl_4$ (LAC) and $Li_{6.6}La_3Zr_{1.6}Ta_{0.4}O_{12}$ (LLZT) powders. Cross-sectional SEM images and relative densities of the (a) LAC and (b) LLZT pellets. The LAC particles were more deformed than the LLZT particles. Impedance plots of the (c) LAC and (d) LLZT pellets at 25 °C normalized by the thickness and area of the pellets for comparison. The conductivities were calculated from the R_{total} values in the figures. Distribution of relaxation times (DRT) spectra were calculated from the impedance plots of the green compacts of (e) LAC and (f) LLZT. Insets: pie charts representing the contributions of the bulk and grain boundaries to the total resistance. The grain boundary resistance in the LAC green compact is negligible, in contrast with its major contribution to the resistance of the LLZT green compact.

Impedance plots for the green compact of LAC and LLZT at room temperature are shown in **Figure 3(c)** and **(d)**. A distorted semicircle and a spike were observed in both plots. This spike stems from Li^+ blocking behavior at the electrolyte/electrode interfaces[40], and thus the semicircles correspond to the ionic transport in the green compacts. The polarization test shown in

Supporting Figure S1 also indicates the small contribution of the electrical conductivity in the material. The total resistance of the semicircles, R_{total}, in the figures contains the components of bulk and grain-boundary resistances in the green compacts. Total ionic conductivity calculated by R_{total} is 2.1×10^{-5} S cm^{-1} for the LAC green compact, which is twenty times higher than the bulk conductivity of the reported monoclinic LAC (σ_{25} = 1.0×10^{-6} S cm^{-1})[33]. The activation energy of 0.50(6) eV, calculated from the Arrhenius plots shown in **Supporting Figure S2**, is almost the same as that reported for monoclinic LAC (0.47 eV)[33]. The number of Li ion carriers is limited in conventional LAC due to the fully occupied Li sites. The Li ions at metastable sites indicated by NMR measurements (**Figure 2(c)**) reveal the delocalization of Li^+ ions in the conduction pathway, which generates Li^+ ion carriers with adjacent vacancy and significantly contributes to the increase in ionic conductivity. Additionally, the total ionic conductivity for the LAC green compact is much higher than that of the LLZT green compact (5.5×10^{-7} S cm^{-1}). Resistance components were analyzed based on the distribution of relaxation times (DRT)[41,42] to investigate the reason for the conductivity difference. The DRT spectra in both samples shown in **Figure 3(e)** and **(f)** indicate two resistance peaks. Considering the ionic transport in the green compact of the single-phase material, the major peak components at the higher and lower frequency were attributed to resistance in the bulk and grain boundary, respectively. As revealed by the pie charts in the insets of **Figure 3(e)** and **(f)**, the grain boundary resistance in the LAC sample has a small contribution of 7.5% to the total resistance, while the majority of total resistance (> 99%) for the LLZT green compact is attributed to the grain boundary contribution. Thus, the almost negligibly small grain boundary resistance is confirmed for the LAC green compact with good contact among particles, which is one reason for the high conductivity.

Galvanostatic cycle performance of the Li symmetric cells using the solid electrolyte of the mechanochemical synthesized LAC or LLZT green compact are compared in **Figure 4**. The cell using the LAC green compact shows good cycle performance, i.e., almost no increase of the overvoltage and no short-circuiting during 70 charge-discharge cycles at a current density of 0.1 mA cm^{-2}. The over-voltage profile of the LAC cell was constant for more than 160 h, which indicates the inhibition of Li dendrites and possible chemical compatibility with Li metal. Indeed, the impedance plots of the LAC electrolyte sandwiched between stainless steel or Li metal electrodes are compared in **Supporting Figure S3**, indicating the low interfacial resistance between the electrolyte and Li metal electrodes. On the other hand, a large overvoltage is indicated at the same current density condition in the LLZT cell as shown in **Supporting Figure S4**. Moreover, short-circuiting occurred during the 1st cycle in the LLZT cell even at the one tenth current density (0.01 mA cm^{-2}). The impedance plots after the first cycle (**Supporting Figure S5**) show the cell resistance considerably decreases to ~20 Ω, which also indicates Li dendrite growth in the LLZT cell. Therefore, the formability and conductivity of the LAC particle allows for preparation of dense pellets and prevents Li dendrites.

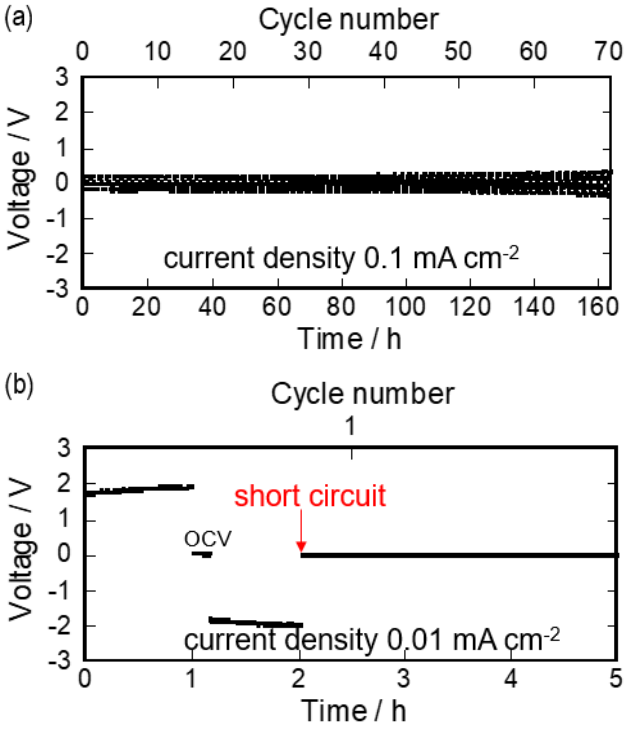

Figure 4. Galvanostatic cycle performance of the Li symmetric cells with solid electrolyte of (a) $LiAlCl_4$ and (b) $Li_{6.6}La_3Zr_{1.6}Ta_{0.4}O_{12}$ green compacts at 25 °C.

In this study, a solid electrolyte material was sought, in which a high-energy-density Li metal electrode can be utilized by simply compressing the electrolyte powders, without sintering processes that lead to problems in electrode/electrolyte materials selection and Li dendrite inhibition. Monoclinic LAC was focused on based on the comprehensive computation results of Li^+ ion migration energy, bulk modulus, and energy above the hull, in addition to consideration of the polarizability and Coulombic interaction. Mechanochemically synthesized monoclinic LAC, in which a few percentages of Li ions are delocalized in the conductive pathway, showed an ionic conductivity 20 times higher than the conventional solid-state synthesized LAC. Moreover, the simple green compacts exhibited much higher performance of Li dendrite inhibition owing to the much higher relative density and stronger grain boundaries than LLZT oxide green compacts. Therefore, this LAC material has revealed the possibility of a Li metal electrode in all-solid-state Li batteries without sintering limits by simply compressing it.

EXPERIMENTAL METHODS

Mechanochemical synthesis and characterization of $LiAlCl_4$

LiCl (99.9%, Kojundo Chemical Laboratory Co., Ltd.) and $AlCl_3$ (99.9%, Wako Chemicals) were mixed at the chemical stoichiometry and placed into a 45 mL ZrO_2 pot with 16 ZrO_2 balls with a diameter of 10 mm. The mixture was ball-milled for 24 hours using a planetary ball mill apparatus (P-7 classicline, Fritsch Japan Co., Ltd.) using a revolution speed of 510 rpm.

The obtained LAC sample was characterized by XRD measurements using a diffractometer (MiniFlex 600, Rigaku) with Cu Kα radiation, and by ^{7}Li MAS-NMR measurements using a spectrometer (JNM-ECA600II, JEOL RESONANCE Co., Ltd.). The MAS spinning speed was 10 kHz in a Φ3.5 mm ZrO_2 rotor. The 90° pulse width and relaxation delay were 5 μs and 1 s, respectively. The sample in the probe was subsequently annealed at 80 °C for 1 h. The entire procedure was conducted in a dry Ar-filled atmosphere.

Preparation and characterization of green compacts

The LAC powder was sandwiched with stainless steel, and uniaxially compressed at a pressure of 382 MPa to form a green compact. Garnet-type LLZT powder (99.9%, Toshima) was used for the comparison. The thickness of the pellets was almost the same at ca. 0.5 mm. The morphology of the cross-sections was investigated using a scanning electron microscope (SEM; JSM-6360LV, JEOL).

The ionic conductivities of the green compacts were measured by the AC impedance method using stainless steel ion-blocking electrodes. A voltage of 300 mV was applied at 25 °C using an electrochemical analyzer (VSP, BioLogic Co.), and the measurement frequency range was set to 10^2 Hz to 10^6 Hz. DRT analysis was performed using Z-Assist software (Toyo Co.) to separate the bulk and grain boundary resistances.[41,42] An inverse-Fourier transformation was applied to the semicircle components of the impedance plots. The resistances were calculated from the complex non-linear least-squares method, fixing the time constant obtained by the DRT analysis.

Li metal electrodes were prepared by pressing Li film (d = 0.25 mm, Furuuchi Chemical Co.) on a Cu substrate (d = 0.02 mm) at 4 MPa and cutting to a diameter of Φ8 mm. Li metal symmetric cells were prepared by putting the electrodes into both sides of the LAC or LLZT pellet. Galvanostatic charge-discharge cycle tests of the cells were conducted at 25 °C using an electrochemical analyzer (VSP, BioLogic Co.). The current density was 0.1 mA cm^{-2} for the LAC cell and 0.01 mA cm^{-2} for the LLZT cell. Open-circuit voltage (OCV) was set between the charge and discharge process for 10 min. The entire procedure was conducted in a dry Ar-filled glovebox.

COMPUTATIONAL METHODS

Computation of energy above hull, bulk modulus, and migration energy for Li-Cl compounds

The Li-Cl compound crystal structures and thermodynamic stability, i.e., energy convex hull,[31] were referred from the *Materials Project* database[26]. The bulk moduli were investigated by first-principles DFT calculations using the Vienna *ab initio* simulation package (VASP)[43] with the projector augmented-wave (PAW) method[44,45] and plane-wave basis set. A generalized gradient approximation (GGA)-type exchange-correlation functional developed by Perdew, Burke, and Ernzernhof and modified for solid materials (PBEsol)[46,47] was used. For crystal structure relaxation and evaluation of the total electron energy, an on-site Coulomb correction (GGA + U) was included to describe the localized electronic states in 3*d* orbitals. U was set for 3*d* states according to the literature[48]. The bulk modulus was obtained by preparing eleven models with the lattice constant from 0.93 to 1.03 times for each structural model, and calculating each total energy using the Murnaghan equation of state[30]. Figure 5 shows the relationship between the volume and energy of the $LiAlCl_4$ structure as an example. The migration energies were calculated by using the BVFF approach based on a percolation theory[23].

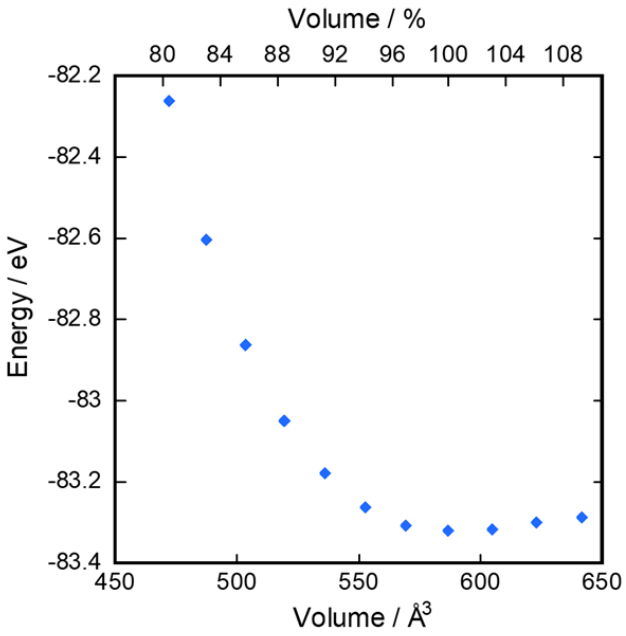

Figure 5. Relationship between the volume and energy calculated by first-principles calculations for the structure of $LiAlCl_4$ in the *Materials Project* database[26]. Bulk moduli were calculated based on the Murnaghan equation of state.

ASSOCIATED CONTENT

Supporting information contains other results of electrochemical measurement for the $LiAlCl_4$ powder-compressed pellet and Li symmetric cells with solid electrolyte of $Li_{6.6}La_3Zr_{1.6}Ta_{0.4}O_{12}$ powder-compressed pellet.

AUTHOR INFORMATION

Author Contributions

The manuscript was written through contributions of all authors. All authors have given approval to the final version of the manuscript.

ACKNOWLEDGMENT

This work was partly supported by the "Advanced Low Carbon Technology Research and Development Program (ALCA)" of the Japan Science and Technology Agency (JST), Japan (since 2013), Grant-in-Aid for Scientific Research (No. 18K19129, No. 18H01707, No. 19H05815, No. 19K15657, No. 19H05812, 20H02436) from Ministry of Education Culture, Sports, Science and Technology, Japan (MEXT), and "Elements Strategy Initiative to Form Core Research Center" (JPMXP0112101003) from MEXT.

M. N. would like to thank the “Materials research by Information Integration Initiative (MI^2I)” project of the “Support Program for Starting Up Innovation Hub” from the Japan Science and Technology Agency (JST) for their support. We also thank the Information Technology Center of Nagoya University for providing computing resources (CX400). Crystal structure diagrams were drawn with Visualization for Electronical and Structural Analysis (VESTA).[49]

ABBREVIATIONS

LAC, $LiAlCl_4$; LLZT, $Li_{6.6}La_3Zr_{1.6}Ta_{0.4}O_{12}$; DFT, density functional theory; BVFF, bond valence force field; DRT, distribution of relaxation times.

REFERENCES

(1) Goodenough, J. B.; Park, K.-S. The Li-Ion Rechargeable Battery: A Perspective. *J. Am. Chem. Soc.* **2013**, 135, 1167–1176.

(2) Xu, K. Nonaqueous Liquid Electrolytes for Lithium-Based Rechargeable Batteries. *Chem. Rev.* **2004**, 104, 4303–4418.

(3) Lin, D.; Liu, Y.; Cui, Y. Reviving the Lithium Metal Anode for High-Energy Batteries. *Nat. Nanotechnol.* **2017**, 12, 194–206.

(4) Xu, W.; Wang, J.; Ding, F.; Chen, X.; Nasybulin, E.; Zhang, Y.; Zhang, J.-G. Lithium Metal Anodes for Rechargeable Batteries. *Energy Environ. Sci.* **2014**, 7, 513–537.

(5) Tanibata, N.; Morimoto, R.; Nishikawa, K.; Takeda, H.; Nakayama, M. Asymmetry in the Solvation–Desolvation Resistance for Li Metal Batteries. *Anal. Chem.* **2020**, 92, 3499–3502.

(6) Goodenough, J. B.; Kim, Y. Challenges for Rechargeable Li Batteries. *Chemistry of Materials*. February 9, 2010, pp 587–603.

(7) Bachman, J. C.; Muy, S.; Grimaud, A.; Chang, H. H.; Pour, N.; Lux, S. F.; Paschos, O.; Maglia, F.; Lupart, S.; Lamp, P.; Giordano, L.; Shao-Horn, Y. Inorganic Solid-State Electrolytes for Lithium Batteries: Mechanisms and Properties Governing Ion Conduction. *Chemical Reviews*. American Chemical Society January 13, 2016, pp 140–162.

(8) Janek, J.; Zeier, W. G. A Solid Future for Battery Development. *Nature Energy*. Nature Publishing Group September 8, 2016.

(9) Li, J.; Ma, C.; Chi, M.; Liang, C.; Dudney, N. J. Solid Electrolyte: The Key for High-Voltage Lithium Batteries. *Adv. Energy Mater.* **2015**, 5, 1401408.

(10) Yu, C.; Ganapathy, S.; Eck, E. R. H. V.; Wang, H.; Basak, S.; Li, Z.; Wagemaker, M. Accessing the Bottleneck in All-Solid State Batteries, Lithium-Ion Transport over the Solid-Electrolyte-Electrode Interface. *Nat. Commun.* **2017**, 8, 1086.

(11) Ohta, N.; Takada, K.; Zhang, L.; Ma, R.; Osada, M.; Sasaki, T. Enhancement of the High-Rate Capability of Solid-State Lithium Batteries by Nanoscale Interfacial Modification. *Adv. Mater.* **2006**, 18, 2226–2229.

(12) Li, Y.; Zhou, W.; Chen, X.; Lü, X.; Cui, Z.; Xin, S.; Xue, L.; Jia, Q.; Goodenough, J. B. Mastering the Interface for Advanced All-Solid-State Lithium Rechargeable Batteries. *Proc. Natl. Acad. Sci. U. S. A.* **2016**, 113, 13313–13317.

(13) Thangadurai, V.; Narayanan, S.; Pinzaru, D. Garnet-Type Solid-State Fast Li Ion Conductors for Li Batteries: Critical Review. *Chemical Society Reviews*. Royal Society of Chemistry July 7, 2014, pp 4714–4727.

(14) van den Broek, J.; Afyon, S.; Rupp, J. L. M. Interface-Engineered All-Solid-State Li-Ion Batteries Based on Garnet-Type Fast Li^+ Conductors. *Adv. Energy Mater.* **2016**, 6, 1600736.

(15) Murugan, R.; Thangadurai, V.; Weppner, W. Fast Lithium Ion Conduction in Garnet-Type Li7La3Zr2O12. *Angew. Chemie Int. Ed.* **2007**, 46, 7778–7781.

(16) Aboulaich, A.; Bouchet, R.; Delaizir, G.; Seznec, V.; Tortet, L.; Morcrette, M.; Rozier, P.; Tarascon, J.-M.; Viallet, V.; Dollé, M. A New Approach to Develop Safe All-Inorganic Monolithic Li-Ion Batteries. *Adv. Energy Mater.* **2011**, 1, 179–183.

(17) Wang, S.; Zhang, Y.; Zhang, X.; Liu, T.; Lin, Y.-H.; Shen, Y.; Li, L.; Nan, C.-W. High-Conductivity Argyrodite Li_6PS_5Cl Solid Electrolytes Prepared via Optimized Sintering Processes for All-Solid-State Lithium–Sulfur Batteries. *ACS Appl. Mater. Interfaces* **2018**, 10, 42279–42285.

(18) Park, K.; Yu, B. C.; Jung, J. W.; Li, Y.; Zhou, W.; Gao, H.; Son, S.; Goodenough, J. B. Electrochemical Nature of the Cathode Interface for a Solid-State Lithium-Ion Battery: Interface between LiCoO2 and Garnet-Li7La3Zr2O12. *Chem. Mater.* **2016**, 28, 8051–8059.

(19) Delaizir, G.; Viallet, V.; Aboulaich, A.; Bouchet, R.; Tortet, L.; Seznec, V.; Morcrette, M.; Tarascon, J.-M.; Rozier, P.; Dollé, M. The Stone Age Revisited: Building a Monolithic Inorganic Lithium-Ion Battery. *Adv. Funct. Mater.* **2012**, 22, 2140–2147.

(20) Han, F.; Yue, J.; Chen, C.; Zhao, N.; Fan, X.; Ma, Z.; Gao, T.; Wang, F.; Guo, X.; Wang, C. Interphase Engineering Enabled All-Ceramic Lithium Battery. *Joule* **2018**, 2, 497–508.

(21) Shen, F.; Dixit, M. B.; Xiao, X.; Hatzell, K. B. Effect of Pore Connectivity on Li Dendrite Propagation within LLZO Electrolytes Observed with Synchrotron X-Ray Tomography. *ACS Energy Lett.* **2018**, 3, 1056–1061.

(22) Ren, Y.; Shen, Y.; Lin, Y.; Nan, C. W. Direct Observation of Lithium Dendrites inside Garnet-Type Lithium-Ion Solid Electrolyte. *Electrochem. commun.* **2015**, 57, 27–30.

(23) Sudo, R.; Nakata, Y.; Ishiguro, K.; Matsui, M.; Hirano, A.; Takeda, Y.; Yamamoto, O.; Imanishi, N. Interface Behavior between Garnet-Type Lithium-Conducting Solid Electrolyte and Lithium Metal. *Solid State Ionics* **2014**, 262, 151–154.

(24) Kato, A.; Yamamoto, M.; Sakuda, A.; Hayashi, A.; Tatsumisago, M. Mechanical Properties of Li_2S–P_2S_5 Glasses with Lithium Halides and Application in All-Solid-State Batteries. *ACS Appl. Energy Mater.* **2018**, 1, 1002–1007.

(25) Canepa, P.; Sai Gautam, G.; Hannah, D. C.; Malik, R.; Liu, M.; Gallagher, K. G.; Persson, K. A.; Ceder, G. Odyssey of Multivalent Cathode Materials: Open Questions and Future Challenges. *Chem. Rev.* **2017**, 117, 4287–4341.

(26) Jain, A.; Ong, S. P.; Hautier, G.; Chen, W.; Richards, W. D.; Dacek, S.; Cholia, S.; Gunter, D.; Skinner, D.; Ceder, G.; Persson, K. A. Commentary: The Materials Project: A Materials Genome Approach to Accelerating Materials Innovation. *APL Materials*. American Institute of Physics Inc. July 18, 2013, p 011002.

(27) Nakayama, M.; Kimura, M.; Jalem, R.; Kasuga, T. Efficient Automatic Screening for Li Ion Conductive Inorganic Oxides with Bond Valence Pathway Models and Percolation Algorithm. *Jpn. J. Appl. Phys.* **2016**, 55, 01AH05.

(28) Tanibata, N.; Kondo, Y.; Yamada, S.; Maeda, M.; Takeda, H.; Nakayama, M.; Asaka, T.; Kitajou, A.; Okada, S. Nanotube-Structured Na2V3O7 as a Cathode Material for Sodium-Ion Batteries with High-Rate and Stable Cycle Performances. *Sci. Rep.* **2018**, 8, 17199.

(29) Takeda, H.; Nakano, K.; Tanibata, N.; Nakayama, M. Novel Mg-Ion Conductive Oxide of μ-Cordierite $Mg_{0.6}Al_{1.2}Si_{1.8}O_6$. *Sci. Technol. Adv. Mater.* **2020**, 21, 131–138.

(30) Murnaghan, F. D. The Compressibility of Media under Extreme Pressures. *Proc. Natl. Acad. Sci. U. S. A.* **1944**, 30, 244–247.

(31) Nakayama, M.; Kanamori, K.; Nakano, K.; Jalem, R.; Takeuchi, I.; Yamasaki, H. Data-Driven Materials Exploration for Li-Ion Conductive Ceramics by Exhaustive and Informatics-Aided Computations. *Chem. Rec.* **2019**, 19, 771–778.

(32) Chen, H.; Adams, S. Bond Softness Sensitive Bond-Valence Parameters for Crystal Structure Plausibility Tests. *IUCrJ* **2017**, 4, 614–625.

(33) Weppner, W. Ionic Conductivity of Solid and Liquid LiAlCl[Sub 4]. *J. Electrochem. Soc.* **1977**, 124, 35.

(34) Kendall, J.; Crittenden, E. D.; Miller, H. K. A Study of the Factors Influencing Compound Formation and Solubility in Fused Salt Mixtures. *J. Am. Chem. Soc.* **1923**, 45, 963–996.

(35) Nakayama, M.; Kotobuki, M.; Munakata, H.; Nogami, M.; Kanamura, K. First-Principles Density Functional Calculation of Electrochemical Stability of Fast Li Ion Conducting Garnet-Type Oxides. *Phys. Chem. Chem. Phys.* **2012**, 14, 10008–10014.

(36) Murugan, R.; Weppner, W.; Schmid-Beurmann, P.; Thangadurai, V. Structure and Lithium Ion Conductivity of Bismuth Containing Lithium Garnets Li5La3Bi2O12 and Li6SrLa2Bi2O12. *Mater. Sci. Eng. B Solid-State Mater. Adv. Technol.* **2007**, 143, 14–20.

(37) ICSD - FIZ Karlsruhe https://www.fiz-karlsruhe.de/de/leistungen/kristallographie/icsd.html (accessed Jun 4, 2018).

(38) Nagel, R.; Wickel, C.; Senker, J.; Lutz, H. D. 6Li and 7Li MAS-NMR Studies on Fast Ionic Conducting Inverse Spinel-Type Li2-2xMg1+xCl4 and Normal Spinel-Type Li2ZnCl4. *Solid State Ionics* **2000**, 130, 169–173.

(39) Hamao, N.; Kataoka, K.; Kijima, N.; Akimoto, J. Synthesis, Crystal Structure and Conductive Properties of Garnet-Type Lithium Ion Conductor Al-Free $Li7-xLa3Zr2-xTaxO12$ ($0 \leq x \leq 0.6$). *J. Ceram. Soc. Japan* **2016**, 124, 678–683.

(40) Murayama, M.; Sonoyama, N.; Yamada, A.; Kanno, R. Material Design of New Lithium Ionic Conductor, Thio-LISICON, in the Li2S-P2S5 System. *Solid State Ionics* **2004**, 170, 173–180.

(41) Schichlein, H.; Müller, A. C.; Voigts, M.; Krügel, A.; Ivers-Tiffée, E. Deconvolution of Electrochemical Impedance Spectra for the Identification of Electrode Reaction Mechanisms in Solid Oxide Fuel Cells. *J. Appl. Electrochem.* **2002**, 32, 875–882.

(42) Sumi, H.; Shimada, H.; Yamaguchi, Y.; Yamaguchi, T.; Fujishiro, Y. Degradation Evaluation by Distribution of Relaxation Times Analysis for Microtubular Solid Oxide Fuel Cells. *Electrochim. Acta* **2020**, 339, 135913.

(43) Kresse, G.; Furthmüller, J. Efficient Iterative Schemes for *Ab Initio* Total-Energy Calculations Using a Plane-Wave Basis Set. *Phys. Rev. B* **1996**, 54, 11169.

(44) Blöchl, P. E. Projector Augmented-Wave Method. *Phys. Rev. B* **1994**, 50, 17953.

(45) Kresse, G.; Furthmiiller, J. Efficiency of Ab-Initio Total Energy Calculations for Metals and Semiconductors Using a Plane-Wave Basis Set. *Comput. Mater. Sci.* **1996**, 6, 15–50.

(46) Perdew, J. P.; Burke, K.; Ernzerhof, M. Generalized Gradient Approximation Made Simple. *Phys. Rev. Lett.* **1996**, 77, 3865.

(47) Perdew, J. P.; Ruzsinszky, A.; Csonka, G. I.; Vydrov, O. A.; Scuseria, G. E.; Constantin, L. A.; Zhou, X.; Burke, K. Restoring the Density-Gradient Expansion for Exchange in Solids and Surfaces. *Phys. Rev. Lett.* **2008**, 100, 136406.

(48) Jain, A.; Hautier, G.; Ong, S. P.; Moore, C. J.; Fischer, C. C.; Persson, K. A.; Ceder, G. Formation Enthalpies by Mixing GGA and GGA + U Calculations. *Phys. Rev. B - Condens. Matter Mater. Phys.* **2011**, 84, 045115.

(49) Momma, K.; Izumi, F.; IUCr. *VESTA* : A Three-Dimensional Visualization System for Electronic and Structural Analysis. *J. Appl. Crystallogr.* **2008**, 41, 653–658.

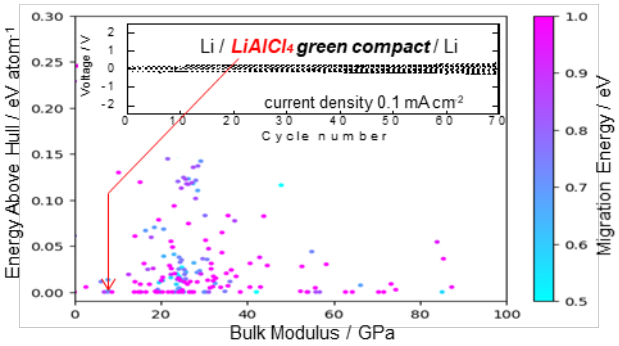

For Table of Contents Only